Highly Functionalizable Penta-Coordinate Iron Hydrogen Production Catalysts with Low Overpotentials

Shawn C. Eady, Tanya Breault[‡], Levi Thompson[‡], Nicolai Lehnert[†]*

[†]Department of Chemistry, University of Michigan, 930 North University, Ann Arbor, Michigan 48109-1055, United States

[‡]Department of Chemical Engineering, University of Michigan, 1221 Beal Avenue, Ann Arbor, Michigan 48109-2102, United States

Supporting Information

Table of Contents.

1. NMR-spectra of selected complexes

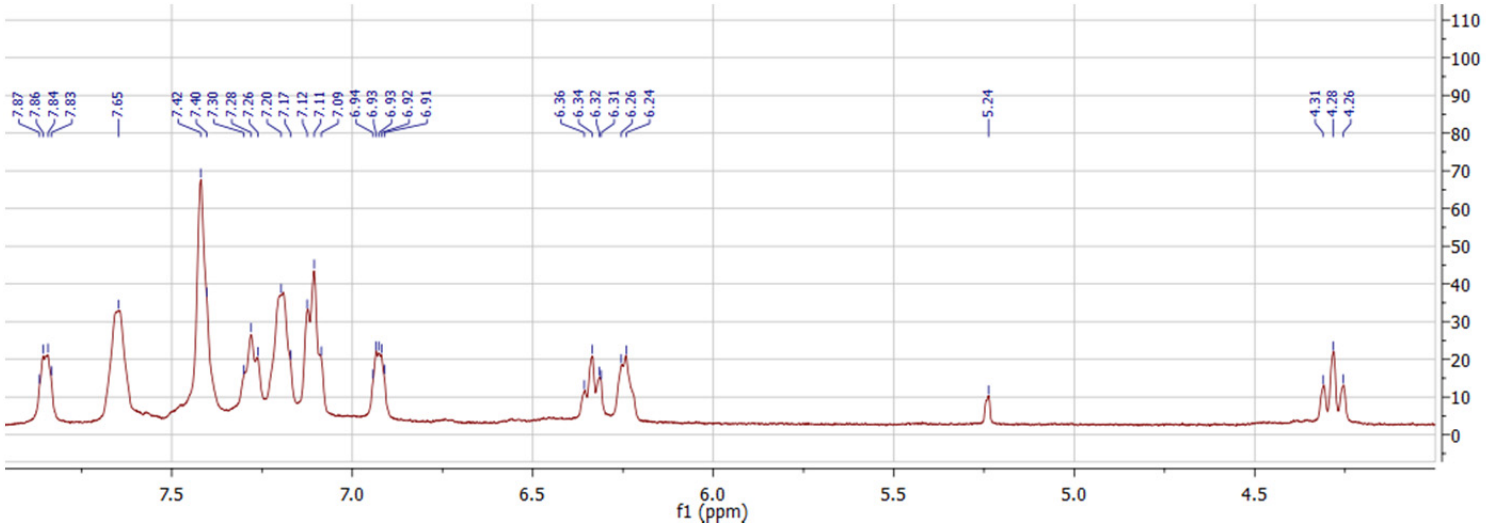

Figure S1. ^{1}H NMR spectra of [Fe($S_2C_6H_4$)((C_6H_5)$_2$PN(p-fluorobenzyl)P(C_6H_5)$_2$)CO] (**5**) in CD_2Cl_2.

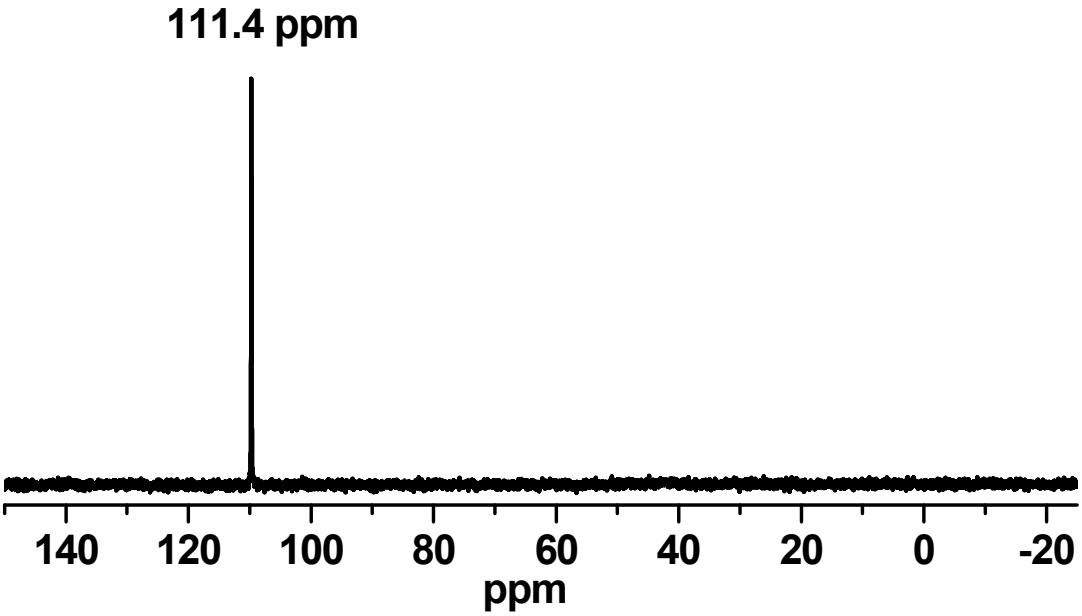

Figure S2. ^{31}P NMR spectra of $[Fe(S_2C_6H_4)((C_6H_5)_2PN(p\text{-fluorobenzyl})P(C_6H_5)_2)CO]$ (**5**) in CD_2Cl_2.

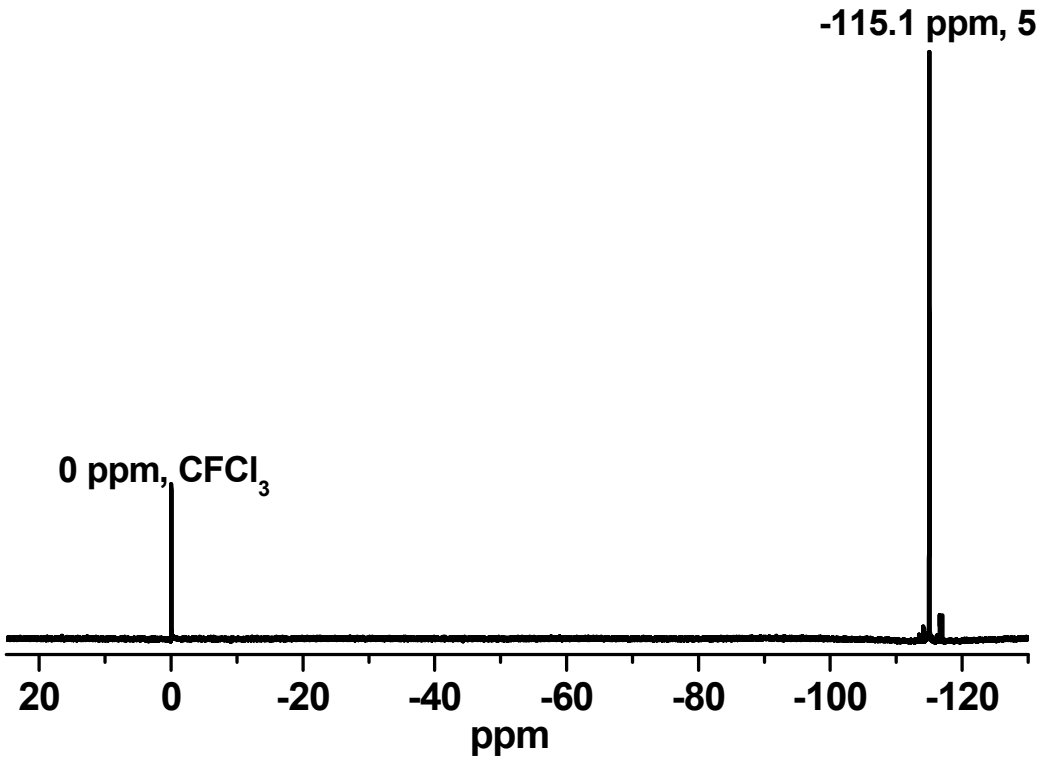

Figure S3. ^{19}F NMR spectra of $[Fe(S_2C_6H_4)((C_6H_5)_2PN(p\text{-fluorobenzyl})P(C_6H_5)_2)CO]$ (**5**) in CD_2Cl_2.

2. IR-Spectra of select complexes

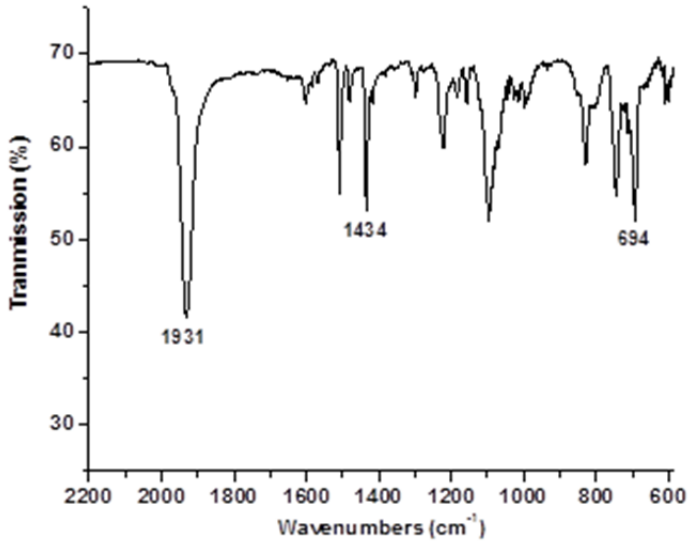

Figure S4. IR spectra of [Fe($S_2C_6H_4$)((C_6H_5)$_2$PN(p-fluorobenzyl)P(C_6H_5)$_2$)CO] (**5**) embedded in KBr matrix.

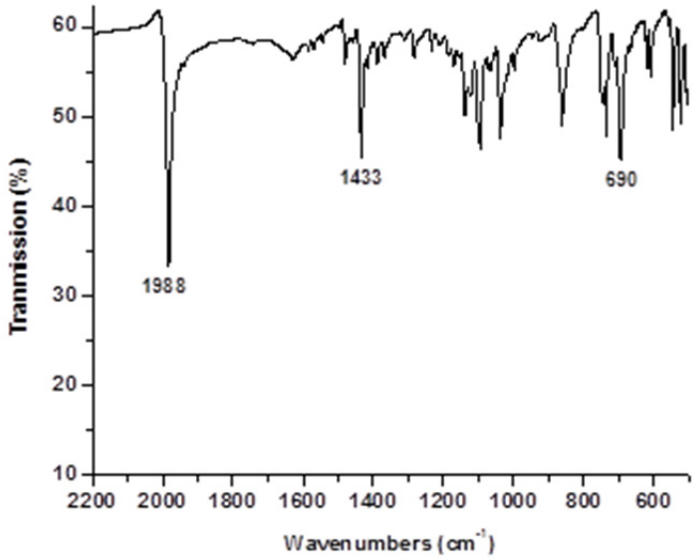

Figure S5. IR spectra of [Co($S_2C_6H_4$)((C_6H_5)$_2$PN(^{i}Pr)P(C_6H_5)$_2$)CO] (**10**) embedded in KBr matrix.

3. Structural comparison of FePNP units

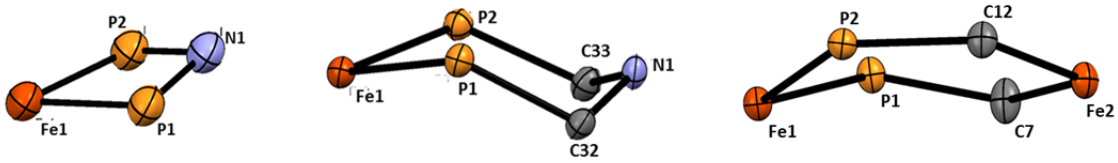

Figure S6. Structural comparison of the FePXP unit for $[Fe(S_2C_6H_4)((C_6H_5)_2PN(^iPr)P(C_6H_5)_2)CO]$ (**1**) (*left)*, $Fe(S_2C_6H_4)((C_6H_5)_2PCH_2N(dep)CH_2P(C_6H_5)_2)(CO)$[1] *(center*), and $[Fe(S_2C_6H_4)((C_6H_5)_2P(FeCp_2)\ P(C_6H_5)_2)(CO)]$ (*right.)*

4. Electrocatalytic studies of pentacoordinate cobalt analogs

In order to obtain further insight into the mechanism and fate of the $[Co(S_2C_6H_4)((C_6H_5)_2PN(^iPr)P(C_6H_5)_2)CO]$, the crude product of **10** was monitored by solution IR spectroscopy upon addition of increasing equivalents of triethylammonium hexafluorophosphate ($Et_3NH\ PF_6$, $pKa_{MeCN} = 18.5$)[1] (**Figure S7**). The observed depletion of the ν(C-O) band at 1993 cm^{-1} at higher acid concentrations with no new signal in the carbonyl range confirmed the decomposition of **10** during electrochemical analysis. These results indicate that the observed catalytic current must in fact correspond to at least two active species in the crude product, and

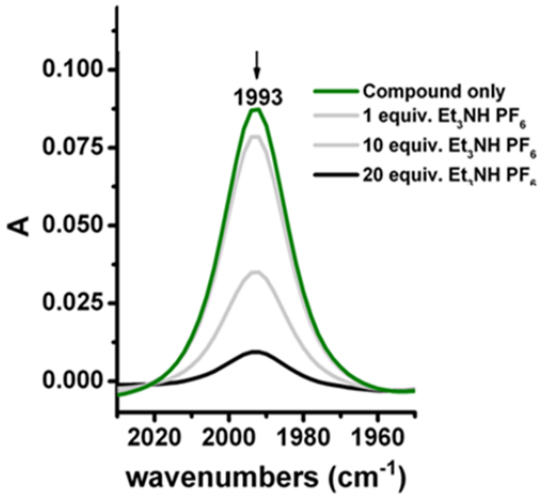

Figure S7. Monitoring of ν(C-O) for the crude product of $[Co((C_6H_5)_2PN(^iPr)P(C_6H_5)_2)(S_2C_6H_4)(CO)]$ (**10**) in acetonitrile (5 mM) with addition of triethylammonium hexafluorophosphate using IR spectroscopy. Under these conditions, decomposition of the Co complex is observed.

that the shifting of the E_{cat} is due to the decomposition and subsided activity of **10** at higher acid concentrations. This hypothesis was further supported by the presence of two redox signals typically found in the crude of **10** (**Figure S8**).

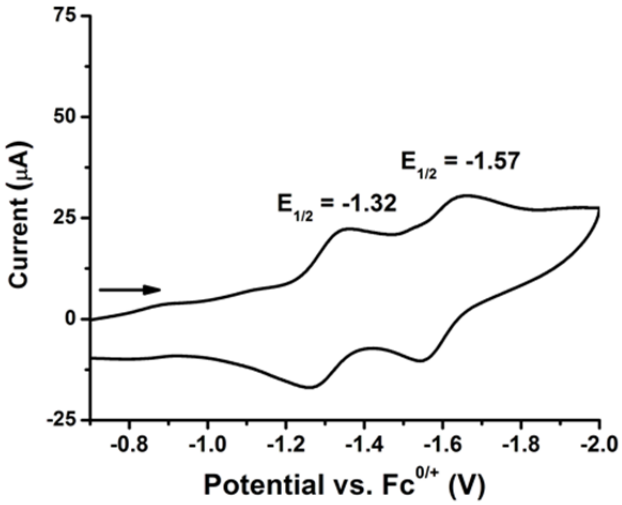

Figure S8. Cyclic voltammogram of $[Co(S_2C_6H_4)((C_6H_5)_2PN(^iPr)P(C_6H_5)_2)CO]$ (**10**) in acetonitrile solution with 0.1 M $(TBA)PF_6$ supporting electrolyte. The working electrode was a glassy carbon disc, the reference was a non-aqueous $Ag/AgNO_3$ (0.01M) electrode, and the auxiliary electrode was a platinum disc electrode. The redox couple with $E_{1/2}$ = -1.32 V was seen to vary in concentration for each batch of compound. Typically the feature was significantly lower in current response than the redox couple with $E_{1/2}$ = -1.57 V and was originally considered an impurity, for better visibility a batch with a larger signal at $E_{1/2}$ = -1.32 V is shown here.

These results prompted us to investigate the second active species in the crude product, which remains active at high acid concentrations, and which has a very high catalytic activity (TOF > 1000 s^{-1}) as estimated with **equation 1**. To determine the identity of this elusive species, extensive column chromatography using various stationary phases and techniques was utilized. Chromatography was found to be generally inefficient for the complete isolation of the second active species; however, electrochemical analysis of all column fractions in the presence of acid allowed for the identification of fractions containing the highest activity levels per fraction mass. In this way, the unknown active species could be concentrated, and subsequently analyzed by ^{31}P NMR and UV-Visible spectroscopy. Surprisingly, the ^{31}P NMR results clearly showed that the major species present in these fractions did not contain the phosphine ligand. Reproduction of

the original synthesis in the absence of diphosphine and CO yielded deep blue cobalt dithiolate compounds. Suspiciously, the UV-Visible spectrum of this compound matches those of the most active column fractions of the crude product of **10**. Electrochemical testing of these cobalt dithiolate compounds under the same conditions as **10** showed a redox wave corresponding to the unknown active species in **Figure S8**, and the same catalytic current response was observed at high acid concentrations as was seen with the crude product of **10** (after the depletion of the penta-coordinate cobalt complex).

At that time, analogous reactivity and synthetic details were reported by Eisenberg and coworkers regarding cobalt bis(dithiolate) H_2 production catalysts.[2] Based on these considerations, it is evident that the unknown active species in our preparations is the cobalt bis(dithiolate) complex $[Co(S_2C_6H_4)_2]^-$. This evidence suggests that these $Co(S_2C_6H_4)_2$-type species are consistent impurities in the crude product of **10** and similar preparations, and that these species are responsible for the sustained catalytic activity observed in Figure 6 at high acid concentrations. In conclusion, pentacoordinate cobalt complexes of formula $[Co(S_2C_6H_4)((C_6H_5)_2PN(^iPr)P(C_6H_5)_2)CO]$ displayed electrochemical responses indicative of hydrogen production catalysis, but instability in acid and under turnover conditions and difficulty in purification discouraged further investigation. Notably, the unstable nature of these complexes was contrasted by the incredible stability of the unintended $[Co(S_2C_6H_4)_2]^-$ byproduct, which remained capable of turnover after long-term air exposure and extensive chromatography.

5. Electrochemistry

Determination of overpotential relative to platinum

Overpotential was determined by the exact method used by Ott and coworkers,[3] and is given relative to the corresponding $E^{Pt}_{1/2}$ obtained on a freshly polished Pt electrode under exactly the

same conditions. Experimental values of $E_{1/2}$ were taken directly from the inflection point of the catalytic waves, as is appropriate for the S-shaped catalytic curves seen for all catalysts investigated here, indicative of kinetic control without substrate limitations. All compounds were observed to have $E_{1/2}$ values at substrate saturation conditions nearly identical ($\pm$0.01 V) to $E_{1/2}$ values observed in the absence of acid. The data regarding overpotential in Ott's work are directly relevant to the complexes reported here since our electrochemical experiments utilized the same solvent and acids (in nearly identical concentration ranges), as well as overall similar catalysts. Specifically, since all catalysts reported here reach activity saturation within roughly 100 equivalents of acetic acid, using 1 mM catalyst concentrations (i.e. acid concentrations do not exceed 0.2 M), the half-wave potential (E_{cat}) observed for platinum at [AcOH] of 0.2 M by Ott and coworkers, -1.48 V vs. $Fc^{0/+}$, was used to calibrate overpotentials for all catalysts reported here.

Determination of overpotential relative to the thermodynamically reversible reduction of AcOH

The overpotential with respect to the thermodynamic limit, i.e. the lowest possible energy at which protons from acetic acid can be reduced, was determined based on work by Artero and coworkers (analogous to the methodology used by Ott and coworkers; see the Supplementary Information in their paper).[3,4] Since the same solvent, acid, and concentration ranges are used compared to Ott and coworkers, only the final equation is given below, which takes into account the exact acid concentration (100 mM), pKa (22.3) and the homoconjugation of acetic acid (since $K_c C_0 >> 1$ at this concentration):

$$E^{\mathrm{t},c}_{1/2(\mathrm{HA/H_2\,,\,AHA^-})} = E^{\circ}_{(\mathrm{H^+/H_2})} - 2.303\frac{RT}{F}\mathrm{p}K_{\mathrm{a(HA)}} + \varepsilon_D + \frac{RT}{2F}\ln(2K_c^2 C_0 C^{\circ}_{\mathrm{H_2}})$$

where $E^{\circ}_{(H^+/H_2)}$ is the standard reduction potential for protons in acetonitrile, proposed to be 0.14 V vs. $Fc^{0/+}$ by Artero et al. Using these values, Ott and coworkers calculated a potential of -1.32 V vs. $Fc^{0/+}$ for the thermodynamically reversible reduction potential of acetic acid protons in acetonitrile. This gives an overpotential estimate of 0.25 V for our catalyst with the lowest overpotential, compound **3**, with an observed half-wave potential of -1.57 V vs. $Fc^{0/+}$.

Catalytic rate constants

Bimolecular rate constants

To allow comparison to the systems reported by Ott and coworkers, bimolecular rate constants for the catalytic reduction of acetic acid was obtained analogously according to **equation 2**:[3]

(1) $$\boldsymbol{I_p = FAC^0_{cat}\sqrt{D}\sqrt{2kC^0_S}}$$

Here, A is 0.031 cm^2 and D is the diffusion coefficient as calculated from cyclic voltammetry data in the absence of acid with the Randles Sevcik equation (for 25°C):

(2) $$\boldsymbol{I_p = 268,600 n^{3/2} A D^{1/2} C_{cat} v^{1/2}}$$

Giving a value of 1 x 10^5 cm^2/s for D. The slope of the plot for I_p vs. $[AcOH]^{1/2}$ (**Figure S7b**) at the highest substrate concentrations (C^0_S) prior to activity saturation are used to obtain rate constants from eqn. 2. The bimolecular rate constants describe the reaction of the one-electron reduced catalyst species with acetic acid based on a two-step mechanism, with the first homogeneous step being rate limiting.[5]

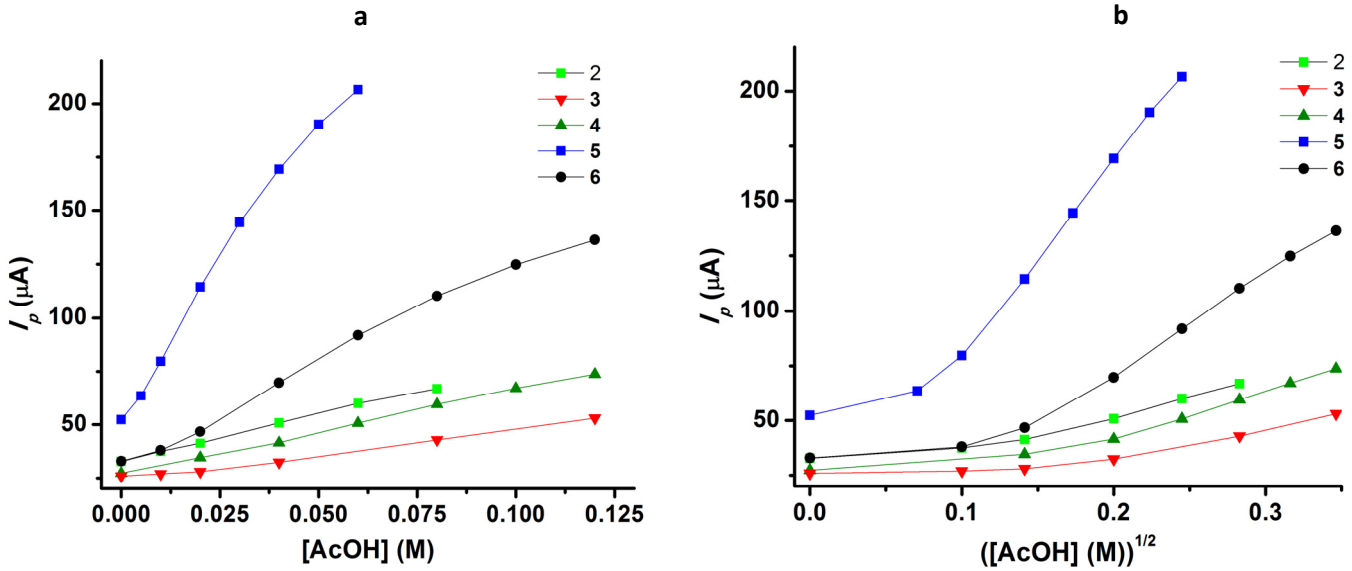

Figure S9. Peak current for **2** (1 mM, light green trace), **3** (1 mM, red trace), **4** (1 mM, green trace), **5** (2 mM, blue trace) and **6** (1 mM, black trace) as a function of [AcOH] (**a**) and $[AcOH]^{1/2}$ (**b**). All experiments were performed in acetonitrile with 0.1 M $(TBA)PF_6$ as supporting electrolyte. The working electrode was a glassy carbon disc, the reference was a non-aqueous $Ag/AgNO_3$ (0.01M) electrode, and the auxiliary electrode was a platinum disc electrode.

TOF estimates from i_{cat}/i_p ratio

Estimations of TOF for all catalyst species were determined according to **equation 1** reported by Bard and Faulkner, corresponding to the ratio of catalytic current in acid-saturated conditions (i_{cat}) to cathodic current in the absence of acid (i_p):[6]

$$\textbf{(1)}\quad \frac{i_{cat}}{i_p} = \frac{2}{0.446}\sqrt{\frac{RTk_{obs}}{Fv}}$$

Here, F is Faraday's constant, ν is scan rate in V/s, and k_{obs} is the estimated rate constant (s^{-1}). Compounds reported here gave a distribution of $i_{cat}/\ i_p$ ratios from 1.22 (**8**) to 4.25 (**6**), corresponding to TOF estimates of 0.28 to 3.51 s^{-1}, respectively.

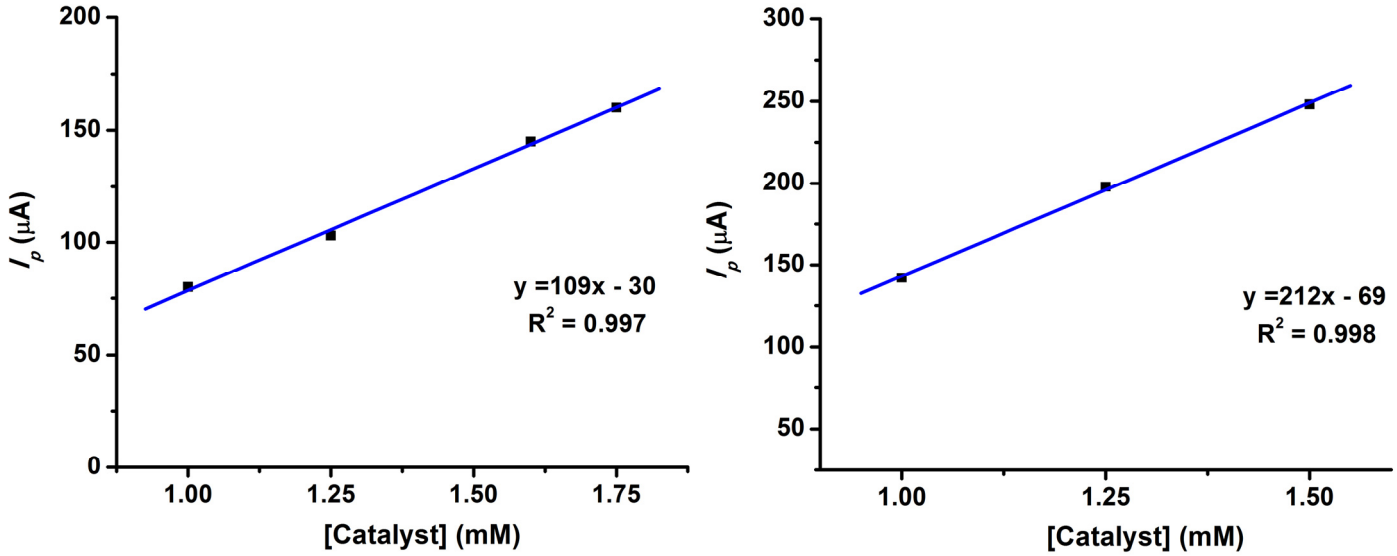

Figure S10. Peak catalytic current for **2** (*left*) and **6** (*right*) with respect to catalyst concentration at acid saturation conditions. All experiments performed in acetonitrile with 0.1 M (TBA)PF_6 as supporting electrolyte. The working electrode was a glassy carbon disc, the reference was a non-aqueous $Ag/AgNO_3$ (0.01M) electrode, and the auxiliary electrode was a platinum disc electrode.

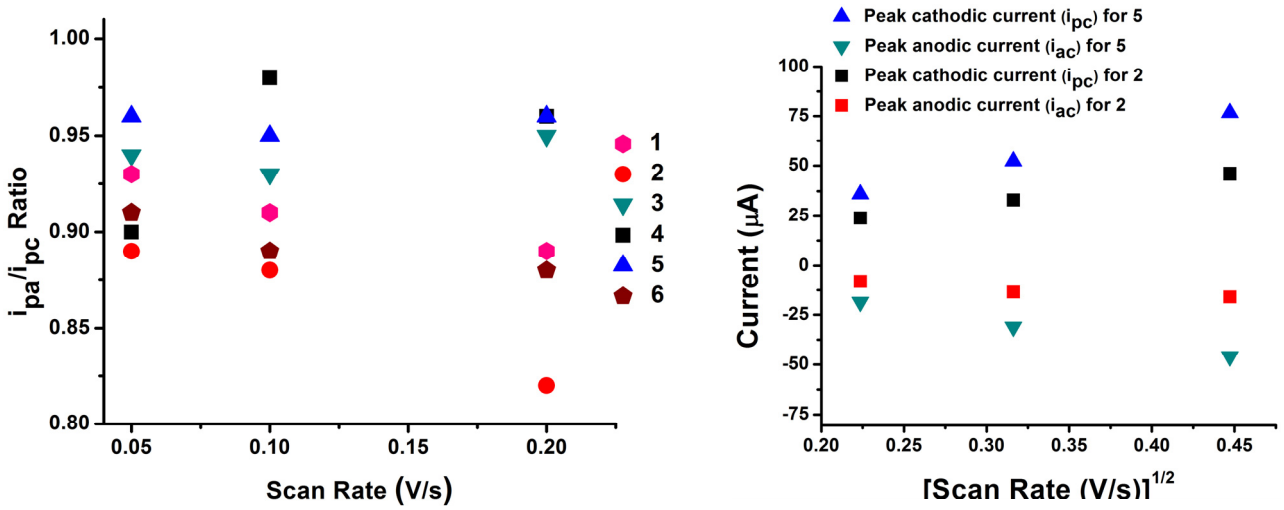

Figure S11. Left: peak anodic:cathodic current ratios for **1** (pink), **2** (red), **3** (grey), **4** (black), **5** (blue) and **6** (wine). Right: variation in peak cathodic/anodic currents as a function of the square root of scan rate for **5** (square) and **2** (circle). Compound **5** is presented as an example of a chemically reversible catalyst ($i_{pa}/i_{pc} \sim 1$), in contrast to compound **2** ($i_{pa}/i_{pc} < 0.9$ at higher scan rates).

6. Comparison of cyclic voltammetry vs. electrolysis observed catalytic rates

The disparity between the rates calculated by cyclic voltammetry and under turnover (electrolysis) conditions is substantial. First of all, this is to a significant degree due to catalyst decomposition during bulk electrolysis, which leads to a constant loss of catalyst in solution (whereas the calculated TOF of 3 h^{-1} is based on the initial catalyst concentration). In addition, one has to consider the rather drastic differences in experimental conditions between CV and bulk electrolysis. In this regard, it is noteworthy that catalyst activities only based on CV data are misleading, and do in no way reflect the catalyst activities that can be achieved under 'real' application conditions, i.e. bulk electrolysis (at least generally speaking). CV estimates for TOFs are only based on the catalysts present in the diffusion layer and activity is estimated based on the diffusion-limited current response with an applied potential which is maintained for only a short time. Migration of catalyst present in the diffusion layer to interact with bulk catalyst is usually negligible in this time frame.

We further explored if some of the difference in TOF between the CV and bulk electrolysis experiments could be due to differences in conditions between these experiments, in particular with respect to the working electrode (carbon felt in electrolysis vs. glassy carbon in cyclic voltammetry). CV studies at a carbon felt electrode were performed to assess if interaction with the electrode material in any way affected the TOF (previously determined at a glassy carbon electrode). These studies show very similar catalyst activity overall, though two differences are notable:

(a) The peak catalytic current to cathodic current ratio (i_{cat}/i_p) is slightly lower at carbon felt (~2.2 instead of 2.7) for compound **1**, although this is within a reasonable variation for an alternative electrode material;

(b) Due to differences in the electrode surface properties of carbon felt versus glassy carbon, the peak catalytic potential is actually more negative for carbon felt compared to glassy carbon (~-2.4 V vs. -1.7 V vs. $Fc^{0/+}$), indicating a further kinetic barrier for electron transfer with the carbon felt electrode. This improves by facilitating diffusion (stirring); however, not to the point where the potential is more positive than ~-2.1 V.

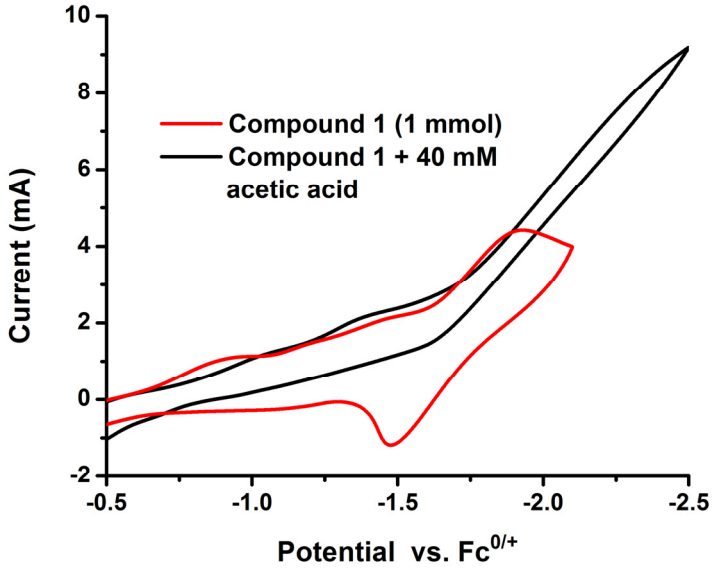

Figure S12. Cyclic voltammogram of **1** at a carbon felt electrode (0.25 cm^2) before and after the addition of acetic acid in acetonitrile solution with 0.1 M (TBA)PF_6 supporting electrolyte. The reference was a non-aqueous Ag/$AgNO_3$ (0.01M) electrode, and the auxiliary electrode was a platinum disc electrode.

These results suggest that the rate achieved under electrolysis conditions (at -1.7 V applied potential) is not at the catalyst maximum rate when the carbon felt electrode is used, which also contributes to the lower TOF observed under bulk electrolysis conditions. At -1.7 V, the current in the presence and absence of acid (**Figure S12**) is approximately the same (i_{cat}/i_p ~1), giving a substantially lower TOF estimate of only 0.2 s^{-1} using **equation 1.** Unfortunately, conduction of bulk electrolysis at more cathodic conditions (< -2.1 V) is not possible, due to the background proton reduction for carbon felt which is more substantial under these conditions.

Finally, the aspect of diffusion also needs to be taken into consideration. One obvious limitation of bulk electrolysis is the fact that the TOF is estimated based on the total amount of catalyst in solution, whereas the hydrogen produced at a given point in time can clearly only account for the catalyst material that is at the electrode surface. Despite having a substantially larger working electrode (3 cm^2 vs. 0.031 cm^2 in CV studies), the limited amount of catalyst at the working electrode in a 20 mL stirred solution must ultimately mean that a rate based on the entire cell's catalyst content will be a drastic underestimate. With respect to decomposition, these complexes are reductively unstable, and even in the absence of diffusion will degrade as evidenced by our spectroelectrochemical IR experiments. A likely pathway for decomposition would be the formation of a dimerized (oligomarized) species upon reduction, which is suggested by the fact that Fe(I) complexes have a tendency to form cluster. Based on these further experiments and considerations, we believe there is sufficient uncertainty and systematic error present in TOF estimates from either CV or bulk electrolysis (in addition to the stability issues of the catalysts) that can account for these differences. It is therefore particularly important when reporting new electrocatalysts that they are tested not only by CV, but actually by bulk electrolysis experiments.

7. X-ray Crystallography

Structural Determination of [Fe($S_2C_6H_4$)((C_6H_5)$_2$PN(^{i}Pr)P(C_6H_5)$_2$)CO] (1)

Brown plates of **1** with dimensions 0.20 x 0.08 x 0.08 mm were grown by slow diffusion of hexane into a dichloromethane solution of the compound at -32 deg. C. A total of 2224 images were collected with an oscillation width of 1.0° in ω. The exposure time was 10 sec. for low angle images, 40 sec. for high angle. The integration of the data yielded a total of 114945 reflections to a maximum 2θ value of 136.48° of which 12773 were independent and 9893 were greater than 2σ (I). The final cell constants (**Table S1**) were based on the xyz centroids of 61985 reflections above 10σ (I). The structure was solved and refined using the space group P2(1)c with Z = 8 for the formula $C_{34}H_{31}NOP_2S_2Fe$, $(CH_2Cl_2)_{0.75}$. There are two independent molecules in the asymmetric unit. Full matrix least-squares refinement based on F^2 converged at R1 = 0.0941 and wR2 = 0.2589 [based on I > 2sigma(I)], R1 = 0.1103 and wR2 = 0.2815 for all data. Additional details are presented in **Table S1** and are given as Supporting Information in a CIF file.

Table S1. Crystal data and structure refinement for **1.**

Identification code	sea
Empirical formula	C34.38 H31.75 Cl0.75 Fe N O P2 S2
Formula weight	683.36
Temperature	85(2) K
Wavelength	1.54178 A
Crystal system, space group	Monoclinic, P2(1)/c
Unit cell dimensions	a = 19.0419(13) A alpha = 90 deg. b = 25.0831(5) A beta = 113.223(8) deg. c = 16.0390(3) A gamma = 90 deg.

Volume	7040.0(5) A^3
Z, Calculated density	8, 1.289 Mg/m^3
Absorption coefficient	6.133 mm^-1
F(000)	2830
Crystal size	0.20 x 0.08 x 0.08 mm
Theta range for data collection	3.08 to 68.24 deg.
Limiting indices	-22<=h<=22, -29<=k<=30, -19<=l<=19
Reflections collected / unique	114945 / 12773 [R(int) = 0.1202]
Completeness to theta = 68.24	99.1 %
Absorption correction	Semi-empirical from equivalents
Max. and min. transmission	0.6397 and 0.3735
Refinement method	Full-matrix least-squares on F^2
Data / restraints / parameters	12773 / 40 / 859
Goodness-of-fit on F^2	1.074
Final R indices [I>2sigma(I)]	R1 = 0.0941, wR2 = 0.2589
R indices (all data)	R1 = 0.1103, wR2 = 0.2815
Extinction coefficient	0.00305(16)
Largest diff. peak and hole	1.210 and -0.677 e.A^-3

Structural Determination of [Fe($S_2C_6H_4$)((C_6H_5)$_2$PN(p-fluorobenzyl)P(C_6H_5)$_2$)CO] (5)

Red plates of **5** with dimensions 0.22 x 0.05 x 0.02 mm were grown by slow diffusion of hexane into a dichloromethane solution of the compound at -32 deg. C. A total of 4118 images were collected with an oscillation width of 1.0° in ω. The exposure time was 3 sec. for the low angle images, 15 sec. for high angle. The integration of the data yielded a total of 47460 reflections to a maximum 2θ value of 136.44° of which 5863 were independent and 5684 were greater than 2σ (I). The final cell constants (**Table S2**) were based on the xyz centroids of 22989 reflections above 10σ (I). The structure was solved and refined using the space group P1bar with Z = 2 for the formula $C_{38}H_{30}NOFP_2S_2Fe$. All non-hydrogen atoms were refined anisotropically with the hydrogen atoms placed in idealized positions. Full matrix least-squares refinement based on F^2 converged at R1 = 0.0336 and wR2 = 0.0926 [based on I > 2sigma(I)], R1 = 0.0344 and wR2 = 0.0936 for all data. Additional details are presented in **Table S2** and are given as Supporting Information in a CIF file.

Table S2. Crystal data and structure refinement for **5**.

Identification code	sed
Empirical formula	C38 H30 F Fe N O P2 S2
Formula weight	717.54
Temperature	85(2) K
Wavelength	1.54178 A
Crystal system, space group	Triclinic, P-1
Unit cell dimensions	a = 9.9659(2) A alpha = 85.660(6) deg. b = 10.6078(2) A beta = 85.253(6) deg. c = 17.0402(12) A gamma = 65.146(5) deg.
Volume	1627.31(12) A^3

Z, Calculated density	2, 1.464 Mg/m^3
Absorption coefficient	6.159 mm^-1
F(000)	740
Crystal size	0.22 x 0.05 x 0.02 mm
Theta range for data collection	4.60 to 68.22 deg.
Limiting indices	-11<=h<=11, -12<=k<=12, -20<=l<=20
Reflections collected / unique	47460 / 5863 [R(int) = 0.0526]
Completeness to theta = 68.22	98.6 %
Absorption correction	Semi-empirical from equivalents
Max. and min. transmission	0.8867 and 0.3444
Refinement method	Full-matrix least-squares on F^2
Data / restraints / parameters	5863 / 0 / 415
Goodness-of-fit on F^2	1.123
Final R indices [I>2sigma(I)]	R1 = 0.0336, wR2 = 0.0926
R indices (all data)	R1 = 0.0344, wR2 = 0.0936
Largest diff. peak and hole	0.393 and -0.657 e.A^-3

Structural Determination of [Co($S_2C_6H_4$)((C_6H_5)$_2$PN(^{i}Pr)P(C_6H_5)$_2$)CO] (10)

Brown plates of **10** with dimensions 0.18 x 0.09 x 0.04 mm were grown by slow diffusion of hexane into a dichloromethane solution of the compound at 25 deg. C. A total of 3429 images were collected with an oscillation width of 1.0° in θ The exposure time was 2 sec. for the low angle images, 8 sec. for high angle. The integration of the data yielded a total of 73268 reflections to a maximum 2θ value of 136.78° of which 5876 were independent and 5164 were greater than 2σ (I). The final cell constants (**Table S3**) were based on the xyz centroids of 29997 reflections above 10σ (I). The structure was solved and refined using the space group P2(1)/n with Z = 4 for the formula $C_{34}H_{31}NOP_2S_2Co$. Full matrix least-squares refinement based on F^2 converged at R1 = 0.0467 and wR2 = 0.1293 [based on I > 2sigma(I)], R1 = 0.0514 and wR2 = 0.1318 for all data. Additional details are presented in **Table S3** and are given as Supporting Information in a CIF file.

Table S3. Crystal data and structure refinement for **10.**

Identification code	sec3
Empirical formula	C34 H31 Co N O P2 S2
Formula weight	654.59
Temperature	85(2) K
Wavelength	1.54178 A
Crystal system, space group	Monoclinic, P2(1)/n
Unit cell dimensions	a = 9.8105(16) A alpha = 90 deg. b = 18.093(3) A beta = 90.131(6) deg. c = 18.118(3) A gamma = 90 deg.
Volume	3216.0(9) A^3
Z, Calculated density	4, 1.352 Mg/m^3

Absorption coefficient	6.549 mm^-1
F(000)	1356
Crystal size	0.18 x 0.09 x 0.04 mm
Theta range for data collection	3.45 to 68.39 deg.
Limiting indices	-11<=h<=11, -21<=k<=21, -21<=l<=21
Reflections collected / unique	73268 / 5876 [R(int) = 0.1018]
Completeness to theta = 68.39	99.7 %
Absorption correction	Semi-empirical from equivalents
Max. and min. transmission	0.771 and 0.514
Refinement method	Full-matrix least-squares on F^2
Data / restraints / parameters	5876 / 0 / 370
Goodness-of-fit on F^2	1.140
Final R indices [I>2sigma(I)]	R1 = 0.0467, wR2 = 0.1293
R indices (all data)	R1 = 0.0514, wR2 = 0.1318
Largest diff. peak and hole	0.502 and -0.944 e.A^-3

8. DFT Calculations

Table S4. DFT-optimized (BP86/TZVP) structure of **1**

	x	y	z
Fe	3.17571	9.37957	6.54388
O	0.69313	9.92739	7.91362
N	1.89266	9.85239	4.00766
C	1.69598	9.71669	7.32404
C	5.4406	8.23227	8.36465
C	6.4892	7.37443	8.7921
H	6.50462	6.46893	8.49878
C	7.51945	7.85603	9.6573
H	8.20355	7.27911	9.97568
C	7.48447	9.22556	10.02284
H	8.10622	9.56669	10.65517
C	6.55054	10.06334	9.45685
H	6.62504	10.99643	9.61161
C	5.48485	9.59679	8.65649
C	0.6053	7.53873	5.1485
C	0.61916	6.17295	5.48898
H	1.44684	5.7039	5.48603
C	-0.52728	5.49571	5.82651
H	-0.48439	4.57516	6.0594
C	-1.75421	6.1579	5.82799
H	-2.55238	5.68634	6.03287
C	-1.80418	7.50737	5.5273
H	-2.63376	7.96639	5.53467
C	-0.62979	8.18963	5.21335
H	-0.67068	9.12272	5.03795
C	3.04548	7.27184	3.69519
C	2.36687	6.38841	2.83145
H	1.42248	6.29837	2.88894
C	3.07379	5.65373	1.90287
H	2.6127	5.06177	1.32213
C	4.43895	5.77413	1.81443
H	4.91526	5.27247	1.16589
C	5.12707	6.63448	2.67374
H	6.07274	6.6997	2.62657
C	4.42395	7.38973	3.59348
H	4.88882	7.99398	4.16095
C	4.24252	11.48831	4.06957
C	4.11337	12.44924	3.06139
H	3.274	12.86011	2.89631
C	5.22107	12.79489	2.3082
H	5.14258	13.45457	1.63019
C	6.44518	12.18537	2.53077
H	7.18886	12.39607	1.97804
C	6.58451	11.27987	3.55516
H	7.43788	10.90613	3.74088
C	5.48127	10.90864	4.32014
H	5.57628	10.2615	5.00847

C	1.80194	12.35995	5.26199
C	0.41367	12.29323	5.19124
H	-0.00558	11.46799	4.97899
C	-0.36667	13.42197	5.43002
H	-1.31379	13.37431	5.36517
C	0.24318	14.59335	5.75724
H	-0.28785	15.36591	5.912
C	1.64484	14.68615	5.87221
H	2.05463	15.50888	6.11983
C	2.41501	13.56494	5.62164
H	3.36151	13.61511	5.69239
C	1.50073	10.18374	2.5912
H	1.41432	11.17703	2.53519
C	0.1571	9.60432	2.24335
H	-0.07411	9.84512	1.32213
H	-0.52048	9.96301	2.85504
H	0.1896	8.62859	2.32736
C	2.53883	9.76736	1.57418
H	3.40561	10.16116	1.81296
H	2.27086	10.08591	0.68539
H	2.61435	8.79163	1.56238
P	2.8062	10.87904	5.01039
P	2.16555	8.38277	4.83794
S	4.35557	7.6669	7.12565
S	4.40207	10.66107	7.84184

Table S5. DFT-optimized (BP86/TZVP) structure of $\mathbf{1}^{-}$

	x	y	z
Fe	-0.6483	-0.42189	-1.02576
O	0.45335	0.25907	-3.66954
N	1.51514	0.75669	0.63773
C	0.0468	0.00025	-2.59665
C	-3.40636	-2.11306	-0.74569
C	-4.34077	-3.12699	-0.45834
H	-3.99154	-4.03773	0.03676
C	-5.68815	-2.97971	-0.80072
H	-6.40003	-3.77776	-0.57197
C	-6.11833	-1.8054	-1.44234
H	-7.16928	-1.68206	-1.7195
C	-5.20161	-0.79245	-1.73317
H	-5.52997	0.12216	-2.23504
C	-3.84033	-0.92479	-1.38455
C	2.76127	-1.14981	-1.23995
C	3.04066	-2.46245	-1.66848
H	2.48671	-3.30235	-1.24238
C	4.00894	-2.70257	-2.64709
H	4.21069	-3.72848	-2.96621
C	4.70878	-1.63601	-3.22576
H	5.46117	-1.82392	-3.99573
C	4.4174	-0.32711	-2.82742
H	4.93813	0.51571	-3.28932
C	3.44756	-0.08786	-1.84837
H	3.20105	0.93579	-1.56383
C	1.67782	-2.06489	1.27607
C	2.96531	-2.56717	1.54388
H	3.80163	-2.29098	0.89856
C	3.18978	-3.41616	2.63277
H	4.19811	-3.79104	2.82838
C	2.1278	-3.78237	3.46913
H	2.30195	-4.44585	4.3203
C	0.84223	-3.29754	3.20407
H	0.00379	-3.58812	3.8421
C	0.61655	-2.44697	2.11698
H	-0.39266	-2.09179	1.89509
C	-0.96861	1.71793	1.83488
C	-0.78117	2.88721	2.59529
H	-0.10132	3.66369	2.23653
C	-1.46116	3.06632	3.80455
H	-1.30094	3.97701	4.38852
C	-2.34655	2.08262	4.2653
H	-2.88154	2.22456	5.20809
C	-2.55235	0.92453	3.50645
H	-3.25713	0.16211	3.8478
C	-1.87462	0.74508	2.29528
H	-2.0488	-0.14605	1.68174
C	0.18382	3.08247	-0.40382

C	1.43058	3.51288	-0.89541
H	2.29453	2.85128	-0.80571
C	1.57089	4.77005	-1.4919
H	2.5508	5.08778	-1.8589
C	0.46448	5.61806	-1.6232
H	0.57276	6.59816	-2.0941
C	-0.7882	5.18925	-1.15969
H	-1.66382	5.83383	-1.27335
C	-0.92963	3.93674	-0.55979
H	-1.91481	3.60692	-0.22106
C	2.39394	1.3016	1.70694
H	2.12858	2.37366	1.74788
C	3.88322	1.21144	1.34474
H	4.48939	1.66481	2.1457
H	4.10704	1.73617	0.40557
H	4.20424	0.165	1.23377
C	2.13932	0.71263	3.10734
H	1.06971	0.72731	3.35247
H	2.67345	1.31183	3.86392
H	2.49745	-0.32345	3.17937
P	-0.09804	1.36039	0.21463
P	1.31025	-0.85236	-0.10649
S	-1.6859	-2.30333	-0.34087
S	-2.67755	0.36562	-1.72436

Table S6. DFT-optimized (BP86/TZVP) structure of **1^- - (CO)**

	x	y	z
Fe	-0.64842	-0.42183	-1.02575
N	1.51522	0.75648	0.63771
C	-3.40668	-2.11264	-0.74562
C	-4.34122	-3.12645	-0.45828
H	-3.9921	-4.03724	0.03681
C	-5.68859	-2.979	-0.80066
H	-6.40056	-3.77698	-0.57193
C	-6.11862	-1.80464	-1.44227
H	-7.16956	-1.68116	-1.7194
C	-5.20178	-0.79179	-1.73308
H	-5.53003	0.12285	-2.23495
C	-3.84051	-0.92431	-1.38448
C	2.76109	-1.1502	-1.23997
C	3.03997	-2.46284	-1.66885
H	2.48562	-3.30263	-1.24303
C	4.00819	-2.70309	-2.64749
H	4.20954	-3.72899	-2.96688
C	4.70848	-1.63665	-3.22584
H	5.46082	-1.82466	-3.99584
C	4.41761	-0.32774	-2.82716
H	4.93868	0.51499	-3.28882
C	3.44782	-0.08837	-1.84808
H	3.20172	0.93531	-1.56328
C	1.67755	-2.06509	1.27608
C	2.96501	-2.56741	1.54395
H	3.80137	-2.29124	0.89867
C	3.18941	-3.4164	2.63285
H	4.19772	-3.79131	2.82851
C	2.12739	-3.78254	3.46919
H	2.30149	-4.44603	4.32038
C	0.84185	-3.29767	3.20409
H	0.00338	-3.5882	3.84209
C	0.61624	-2.4471	2.11697
H	-0.39297	-2.09192	1.89505
C	-0.96833	1.7181	1.83486
C	-0.78017	2.88703	2.59562
H	-0.09973	3.66313	2.23716
C	-1.46016	3.06628	3.80486
H	-1.29939	3.97671	4.38907
C	-2.34626	2.08304	4.26525
H	-2.88123	2.22506	5.20803
C	-2.55274	0.92528	3.50607
H	-3.25804	0.16322	3.84716
C	-1.87502	0.74573	2.29491
H	-2.04968	-0.14513	1.68111
C	0.1843	3.08244	-0.40385
C	1.4312	3.51272	-0.8952
H	2.29509	2.85107	-0.80525

C	1.57173	4.76985	-1.49172
H	2.55174	5.08749	-1.85853
C	0.46541	5.61793	-1.62332
H	0.57387	6.598	-2.09425
C	-0.7874	5.18924	-1.16005
H	-1.66295	5.83388	-1.27394
C	-0.92906	3.93677	-0.56012
H	-1.91433	3.60705	-0.22156
C	2.3941	1.30126	1.7069
H	2.12887	2.37335	1.74787
C	3.88337	1.21092	1.34473
H	4.48958	1.66412	2.14575
H	4.10729	1.73571	0.40562
H	4.20425	0.16445	1.23366
C	2.13939	0.7123	3.1073
H	1.06974	0.72683	3.35227
H	2.67332	1.31162	3.86392
H	2.49767	-0.32372	3.17943
P	-0.09784	1.36042	0.21461
P	1.31011	-0.85254	-0.10653
S	-1.68626	-2.30312	-0.34076
S	-2.67759	0.36599	-1.72426

9. References

(1) Coetzee, J. F. In *Progress in Physical Organic Chemistry*; John Wiley & Sons, Inc.: 2007, p 45.
(2) McNamara, W. R.; Han, Z.; Yin, C.-J.; Brennessel, W. W.; Holland, P. L.; Eisenberg, R. *Proc. Natl. Acad. Sci. USA* **2012**, *109*, 15594.
(3) Beyler, M.; Ezzaher, S.; Karnahl, M.; Santoni, M.-P.; Lomoth, R.; Ott, S. *Chem. Commun.* **2011**, *47*, 11662.
(4) Fourmond, V.; Jacques, P.-A.; Fontecave, M.; Artero, V. *Inorg. Chem.* **2010**, *49*, 10338.
(5) Savéant, J.-M. In *Elements of Molecular and Biomolecular Electrochemistry*; John Wiley & Sons, Inc.: 2006, p 78.
(6) Bard, A. J.; Faukner, L. R. *Electrochemical Methods: Fundamentals and Applications*; 2nd edition ed., 2000.